nature machine intelligence

Article

https://doi.org/10.1038/s42256-024-00853-3

Coordinate-based neural representations for computational adaptive optics in widefield microscopy

Received: 23 July 2023

Accepted: 10 May 2024

Published online: 24 June 2024

Check for updates

Iksung Kang[1,7] ✉, Qinrong Zhang[1,6,7] ✉, Stella X. Yu[2] & Na Ji[1,3,4,5]

Widefield microscopy is widely used for non-invasive imaging of biological structures at subcellular resolution. When applied to a complex specimen, its image quality is degraded by sample-induced optical aberration. Adaptive optics can correct wavefront distortion and restore diffraction-limited resolution but require wavefront sensing and corrective devices, increasing system complexity and cost. Here we describe a self-supervised machine learning algorithm, CoCoA, that performs joint wavefront estimation and three-dimensional structural information extraction from a single-input three-dimensional image stack without the need for external training datasets. We implemented CoCoA for widefield imaging of mouse brain tissues and validated its performance with direct-wavefront-sensing-based adaptive optics. Importantly, we systematically explored and quantitatively characterized the limiting factors of CoCoA's performance. Using CoCoA, we demonstrated in vivo widefield mouse brain imaging using machine learning-based adaptive optics. Incorporating coordinate-based neural representations and a forward physics model, the self-supervised scheme of CoCoA should be applicable to microscopy modalities in general.

Non-invasive and with subcellular resolution, optical microscopy has become an indispensable tool for biomedical research. However, sample heterogeneity and optics imperfections can introduce optical aberration and degrade image quality. Adaptive optics (AO)[1–3] techniques can be used to restore ideal imaging performance by measuring and correcting these aberrations. Conventional AO methods require specialized hardware. Direct-wavefront-sensing-based AO (DWS AO)[4–9], for example, utilizes a wavefront sensor (for example, a Shack–Hartmann sensor) for aberration measurement and a corrective device (for example, a deformable mirror) for aberration correction, increasing the complexity and overall cost of a microscope. For indirect wavefront-sensing AO methods[1–3], a corrective device is still required for wavefront correction.

Machine learning has recently emerged as a promising alternative to hardware-based AO. Supervised machine learning methods can estimate optical aberration from an experimentally measured point spread function (PSF), without the need for wavefront sensors, after a training process that involves learning a nonlinear inverse operator parametrized with neural network weights[10–18]. These approaches require an external training dataset that is either generated through simulations[10,13,14,17,18] or acquired experimentally[11,12,15]. However, to date, there is no well-established learning method for extended structures,

[1]Department of Molecular and Cell Biology, University of California, Berkeley, Berkeley, CA, USA. [2]Department of Electrical Engineering and Computer Science, University of Michigan, Ann Arbor, MI, USA. [3]Department of Physics, University of California, Berkeley, Berkeley, CA, USA. [4]Helen Wills Neuroscience Institute, University of California, Berkeley, Berkeley, CA, USA. [5]Molecular Biophysics and Integrated Bioimaging Division, Lawrence Berkeley National Laboratory, Berkeley, CA, USA. [6]Present address: Department of Biomedical Engineering, City University of Hong Kong, Kowloon, Hong Kong. [7]These authors contributed equally: Iksung Kang, Qinrong Zhang. ✉e-mail: iksung.kang@berkeley.edu; qzhan32@cityu.edu.hk

and a corrective device is still required to correct for optical aberration for high-resolution imaging.

Here we describe a self-supervised machine learning algorithm called CoCoA, which stands for coordinate-based neural representations for computational adaptive optics, for joint estimation of wavefront aberration and three-dimensional structural recovery. Although self-supervised learning approaches have been previously used for denoising[19–23], blind deconvolution[24], two-dimensional (2D) phase imaging[25–27] and tomography[28–31], here a self-supervised scheme is described for computational AO in fluorescence microscopy. CoCoA takes a three-dimensional (3D) aberrated image stack as input and returns the estimated aberration and underlying structures. Representing a notable departure from the existing supervised machine learning approaches, CoCoA does not require any external supervision or external training datasets. Furthermore, CoCoA retrieves underlying features purely through computation, eliminating the need for a corrective device.

Similar to classical image deblurring problems[24,32–35], extracting wavefront and structural information from an aberrated 3D image stack is a highly ill-posed inverse problem, because there are more unknown parameters than independent measurements. To address the severe ill-posedness, CoCoA incorporated a forward model for image formation into the optimization process, obtained Zernike coefficients as a one-dimensional vector during the optimization process and used a multi-layer perceptron (MLP) with Fourier feature mapping (FFM) to represent complex structures. With MLPs as effective universal function approximators due to their nonlinearity[36–38] and FFM ensuring faster convergence to the optimal mapping from coordinates to structure[39,40], CoCoA carefully controlled the physical size of features reconstructed by neural networks to avoid overfitting to noise while still representing the structure accurately to an iterative non-blind baseline method[41] based on the Richardson–Lucy algorithm[42,43].

Using DWS AO to acquire the ground-truth wavefront aberration, we demonstrated that CoCoA can accurately estimate aberration and retrieve 3D structural information from fixed mouse brain slices. Importantly, we characterized the performance limits of CoCoA in terms of image signal-to-noise ratio (SNR) and signal-to-background ratio (SBR). Finally, using CoCoA, we demonstrated in vivo application of machine learning-based AO for widefield microscopy in the mouse brain.

Results

CoCoA, self-supervised learning algorithm for computational AO

We implemented CoCoA, a self-supervised machine learning algorithm, for widefield fluorescence microscopy. CoCoA takes a single 3D image stack as input and outputs estimations of both the underlying 3D structure and the optical aberration present (Fig. 1a). Designed to reproduce the input image stack using a neural network model, CoCoA adjusts its parameters to identify the structure and aberration that give rise to a reproduced image stack most closely resembling the input (Fig. 1a). This process is referred to as self-supervised learning, as CoCoA learns directly from the input image stack itself without requiring labelled examples. Requiring no external supervision, CoCoA differs from existing supervised machine learning methods.

To address the challenge of representing complex structure such as neuronal processes, we employed coordinate-based neural representations[30,40,44,45] that use an MLP as a universal function approximator (Supplementary Fig. 1). The MLP is defined by a set of parameters denoted as θ, representing the weights of the neural network. It employs FFM to achieve rapid convergence towards the optimal mapping from coordinates $\mathbf{r}$ to the representation of the 3D structure s. This technique allows for the incorporation of higher spatial-frequency details into the resulting representation, where the mapping can be expressed as $s = \mathcal{T}_\theta(\mathbf{r})$, and $\mathcal{T}_\theta$ includes a Fourier-type radial encoding scheme (Supplementary Note).

CoCoA also integrates a forward model for image formation into the optimization process. The model serves as a physics prior, imposing a constraint that the solution needs to satisfy the embedded mathematical model. For estimating aberration, we incorporated parameters of our microscope, including back pupil diameter, numerical aperture of the objective lens, voxel size and emission wavelength λ, into the forward model. We also opted to estimate the one-dimensional-vector Zernike coefficients that represent the optical aberration at the back pupil plane.

By integrating the coordinate-based neural representations and imaging-system-informed forward model, both network-structure and physics priors were used to regularize the solution space and reduce ill-posedness. As a result, we achieved accurate estimation of both the 3D structures and optical aberration from a single image stack.

The PSF of widefield microscopy, or equivalently the image of a sub-diffraction-limit point object, is defined as

$$h = \left| \mathcal{F}\left[G(\xi,\eta)\, \mathrm{e}^{-2\pi \mathrm{i} z \sqrt{\left(\frac{n_0}{\lambda}\right)^2 - \xi^2 - \eta^2}} \right] \right|^2 . \tag{1}$$

Here, $G(\xi,\eta) = P(\xi,\eta)\,\mathrm{e}^{\mathrm{i}\varphi}$ is the complex pupil function; $P(\xi,\eta)$ describes the circular aperture of the objective lens; φ, the cumulative optical aberration at the objective lens pupil plane, equal to $\sum_{n,m} \alpha_n^m Z_n^m(\xi,\eta)$, the summation of Zernike modes Z_n^m with coefficients α_n^m following the American National Standards Institute standard; $\mathcal{F}$ is the two-dimensional Fourier transform with respect to the pupil coordinates ξ and η; and n_0 is the refractive index of the medium.

Given the parameterized structure $s = \mathcal{T}_\theta(\mathbf{r})$ and the PSF h, CoCoA computes the estimated 3D image stack $\hat{g}$ following the forward model for image formation using the convolution operator $*$ as

$$\hat{g} = \mathcal{T}_\theta(\mathbf{r}) * h\left(\mathbf{r};\, \alpha_n^m\right). \tag{2}$$

It then compares $\hat{g}$ with the experimentally acquired image stack g and performs iterative updates on both the structure (via θ) and the PSF (via α_n^m) to minimize a user-defined loss function $\mathcal{L}$:

$$\mathcal{L}\left(\hat{g}, g;\, \theta, \alpha_n^m\right) = 1 - \mathrm{SSIM}(\hat{g}, g) + \mathcal{R}(\mathcal{T}_\theta(\mathbf{r})). \tag{3}$$

In equation (3), SSIM stands for structural similarity index metric, a widely accepted loss function[17,27,46,47], which computes the similarity between the estimated 3D image stack $\hat{g}$ and the input g. $\mathcal{R}(\mathcal{T}_\theta(\mathbf{r}))$ is a regularizer that incorporates prior information on the spatial piecewise smoothness and distribution of voxel values of the structure $\mathcal{T}_\theta(\mathbf{r})$.

The final outputs are the estimated Zernike coefficients α_n^m, which allow CoCoA to estimate optical aberration, as well as the neural network weights θ, from which the underlying 3D structure s is obtained (Fig. 1b). Together, the architecture of CoCoA eliminates the need for both a wavefront sensor and a corrective device. This joint estimation capability also sets CoCoA apart from existing supervised deep learning methods.

To characterize the performance of CoCoA, we utilized a widefield microscope equipped with an AO module composed of a wavefront sensor and a deformable mirror (DM) (Fig. 1c and Supplementary Fig. 2). This system measured aberration in the emission path using DWS. With two-photon fluorescence excitation, we generated a 3D-confined 'guide star' in the sample and directed its emitted fluorescence to a Shack–Hartmann (SH) wavefront sensor after descanning[8,9]. The SH sensor used a lenslet array to segment and focus the wavefront onto a camera, creating a 2D array of foci. From local phase slopes calculated from foci displacements relative to an aberration-free condition, we were able to reconstruct the aberrated wavefront. To correct the

https://doi.org/10.1038/s42256-024-00853-3

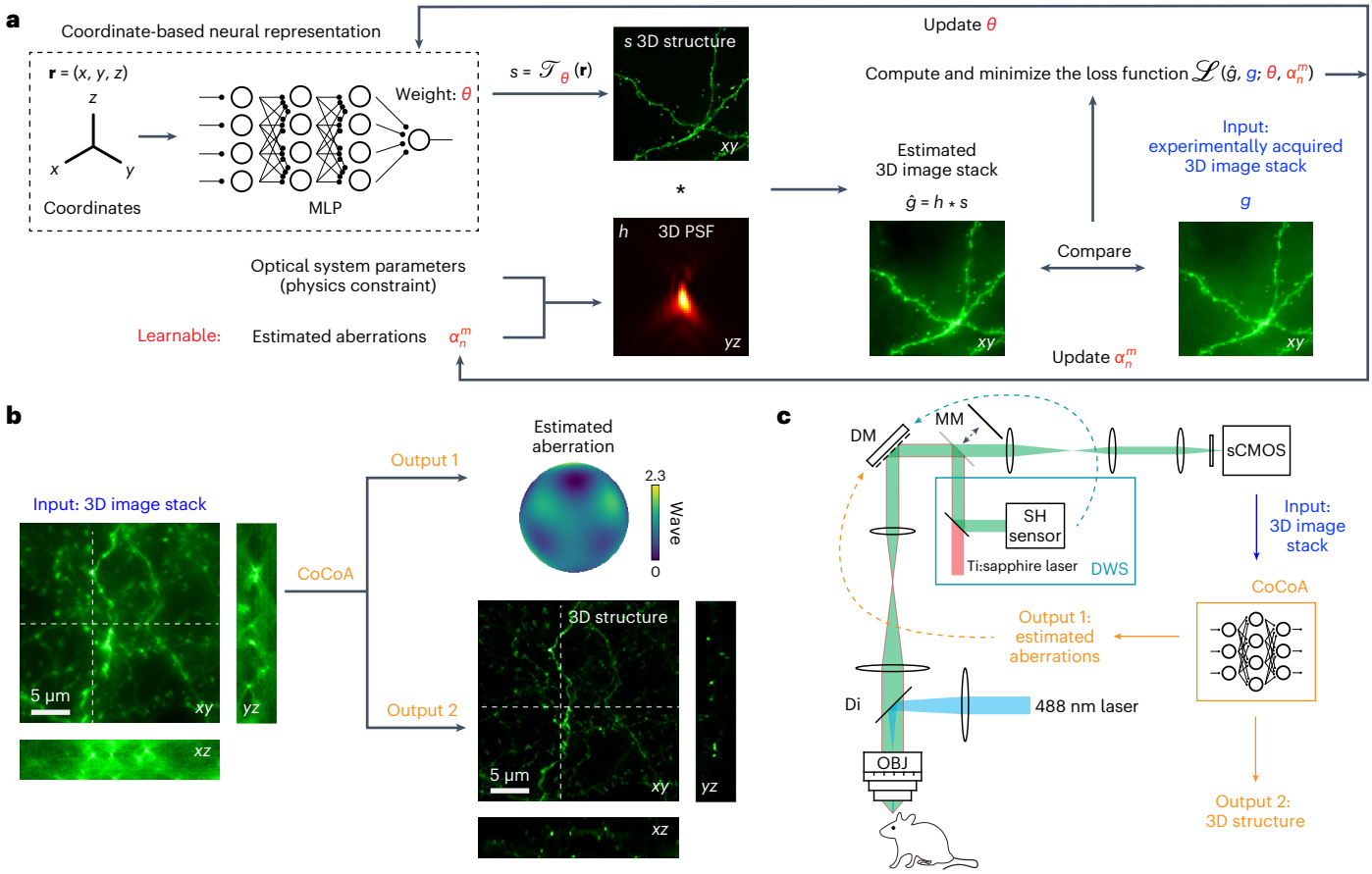

Fig. 1 | CoCoA in widefield imaging. a, CoCoA's self-supervised machine learning framework iteratively updates both the 3D structure s, represented by an MLP with learnable weights θ, through a Fourier-type radial encoding scheme $\mathcal{T}_\theta$ and the 3D PSF h, calculated from optical system parameters and learnable Zernike coefficients α_n^m. CoCoA minimizes a loss function $\mathcal{L}$ by comparing the image stack computed as the convolution (denoted as *) of estimated s and h ($\hat{g}$) with the experimentally acquired 3D image stack g. See Supplementary Note and Supplementary Fig. 1 for details. **b**, CoCoA takes an experimentally acquired 3D image stack as input and outputs both estimated aberrations and 3D structural information. **c**, Schematics of our widefield imaging system equipped with a SH sensor and a two-photon fluorescence guide star (generated by a Ti:sapphire laser) for DWS and a DM for hardware-based aberration correction. See Supplementary Fig. 2 for detailed optical path.

aberration, whether measured via DWS or estimated by CoCoA, we applied the opposite corrective wavefront to the DM, which modified the fluorescence wavefront before image formation on the camera. For some experiments, we also used the DM to introduce known artificial aberration to test CoCoA's performance at different imaging regimes.

One important aspect of this work was to validate the accuracy of CoCoA in aberration estimation and structural recovery, as detailed below. For aberration estimation, we used the wavefront measured by DWS as the ground truth and compared CoCoA and DWS wavefronts, as well as their Zernike decompositions. For structural recovery, we compared the performance of CoCoA with the Richardson–Lucy deconvolution (RLD) algorithm[42,43], a widely used computational technique and focused on how they recovered fine neuronal features such as dendrites and dendritic spines in the brain both in vitro and in vivo.

Implementation and two-stage learning of CoCoA

The Supplementary Note provides detailed information for the neural network architecture, hyperparameter selection and post-processing, in Supplementary Figs. 1, 3 and 4, respectively, and for sampling in Supplementary Figs. 5 and 6 and Supplementary Table 1.

From an input 3D image stack, CoCoA returns an estimated 3D structure, which in coordinate-based neural representations is expressed as a highly nonlinear function parameterized by the MLP weights θ with radial Fourier feature mapping[30]. In our implementation, the MLP received the radially encoded coordinates; it consisted of nine linear layers with skip connections (Supplementary Fig. 1). In addition to optimizing the structural parameters θ, for aberration estimation, CoCoA optimized the learnable coefficients α_n^m associated with the 17 Zernike polynomials from primary astigmatism to pentafoil, excluding defocus, following the American National Standards Institute standard.

In practice, we implemented CoCoA's self-supervised learning in two stages (Supplementary Fig. 7a). In the first stage, we prepared a base model of the structure $\mathcal{T}_\theta(\boldsymbol{r})$ alone (that is, without modelling the image formation process in equation (2)). Starting with θ randomly chosen from a uniform distribution, we fitted the MLP network to the input image stack g (normalized to have its voxel values between 0 and 1) using the loss function $\tilde{\mathcal{L}}$:

$$\tilde{\mathcal{L}}(\tilde{g}, g; \theta) = 1 - \mathrm{SSIM}(\tilde{g}, cg)\,(c > 1),\ \tilde{g} = \mathcal{T}_\theta(\boldsymbol{r})\,. \tag{4}$$

We utilized the Adam optimizer[48] for 400 iterations, starting with an initial rate of 10^{-2} and updated the learning rate using a cosine annealing learning rate schedule. At the end of Stage 1, the MLP learned network weights θ' that reproduced a scaled version of the input image stack.

In the second stage, starting with weights θ' preconditioned during the first stage, the MLP network weights were fine-tuned to generate a 3D structure and the Zernike coefficients α_n^m optimized, so that the 3D image stack $\hat{g}$ computed from equation 2 best resembled the input image stack g, with $\mathcal{L}$ (equation (3)) as the loss function. For the MLP

https://doi.org/10.1038/s42256-024-00853-3

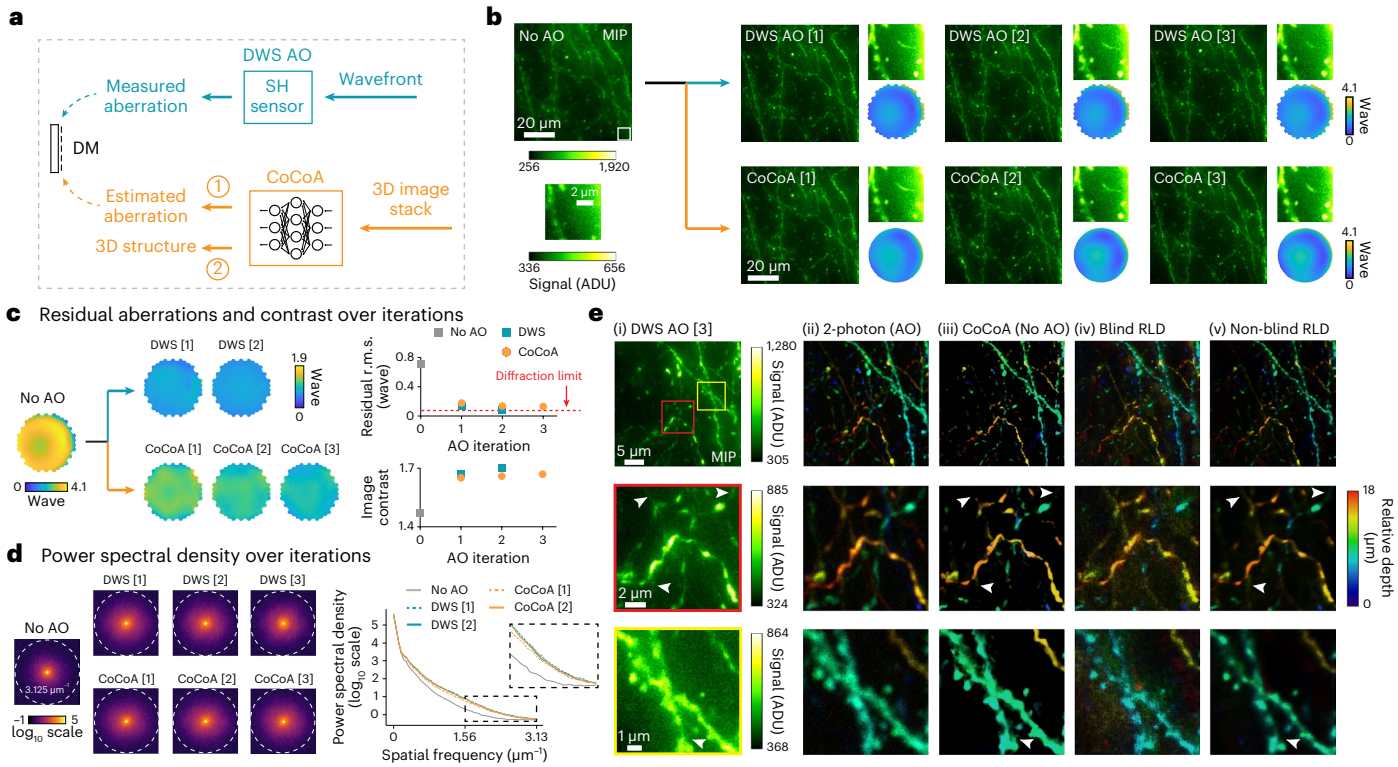

Fig. 2 | CoCoA provides accurate online aberration and structure estimations as validated by DWS and non-blind RLD. a, Schematics of online aberration correction. Cyan: a SH sensor receives a wavefront and measures wavefront aberration. Orange: CoCoA receives a 3D image stack and outputs estimated aberration and 3D structure. Corrective wavefront from either DWS or CoCoA is applied to a DM for online aberration correction. **b**, MIPs of 20-μm-thick image stacks ($80 \times 80 \times 20\ \mu m^3$) acquired without and with aberration correction by DWS (top) and CoCoA (bottom) over iterations, respectively. Insets: zoomed-in views (white box) and corrective wavefronts. ADU, analog-to-digital unit. **c**, Residual aberration and image contrast after DWS- and CoCoA-based corrections over iterations. Left: residual aberration measured with DWS; top right: r.m.s. values of residual aberrations; bottom right: image contrast computed as the ratio between the 99th percentile and the 1st percentile pixel values of insets in **b**. **d**, Spatial-frequency representations of images in **b** and their radially averaged profiles. Inset: zoomed-in view of a mid-to-high spatial-frequency region. Dashed circle: diffraction limit ($3.125\ \mu m^{-1}$). **e**, MIPs of image stacks ($34 \times 34 \times 18\ \mu m^3$) acquired with widefield (i) and two-photon (ii) fluorescence microscopy after DWS AO. MIPs of reconstructed 3D structures (colour-coded by depth) by CoCoA (iii), blind RLD (iv) and non-blind RLD (v) from 'No AO' images.

network, we used an initial learning rate of 5×10^{-3}. For the Zernike coefficients, we started with α_n^m randomly initialized from a uniform distribution and an initial learning rate of 10^{-2}. We employed the same learning rate schedule and optimizer as in the first stage and iteratively updated the learnable parameters by automatic differentiation on the loss function. A machine with an NVIDIA Volta 100 graphics processing unit and an Intel Xeon Gold 6248 central processing unit was used for computation (see Supplementary Table 2 for hyperparameter selection, experimental settings and computation times). Code is designed and developed with PyTorch[49] and is publicly available at https://github.com/iksungk/CoCoA.

We found that CoCoA's performance benefited greatly from having the first stage of base model preparation. Starting the Stage 2 training from θ' rather than randomly initialized weights substantially reduced artefacts and improved the quality of both the structure and aberration estimation (Supplementary Fig. 7b). Additional analysis indicated that a base model prepared from a generic fluorescence image stack can be used for Stage 2 optimization for inputs of a different sample type (Supplementary Fig. 7c–e and Supplementary Note). Therefore, once a base model is available, the first stage of the two-stage learning process may be omitted for other input image stacks.

Aberration estimation and structure recovery by CoCoA

We first tested CoCoA's performance on simulated data. CoCoA accurately extracted structures from 3D bead images of sufficient signal-to-noise ratios (Supplementary Fig. 8). It also accurately estimated aberrations from images of single isolated beads as well as images of extended objects including 3D-distributed beads and neuronal processes (Supplementary Fig. 9). Compared with PhaseNet, a supervised machine learning method[14], CoCoA-estimated aberration at substantially higher accuracy for all sample types but especially for complex extended objects (for example, neuronal processes), giving confidence to its successful application to real-life images of biological samples.

We validated the efficacy of CoCoA with widefield fluorescence microscopy imaging of dendritic structures in fixed mouse brain slices (Thy1-GFP line M; Fig. 2). To introduce aberration similar to those typically induced by a glass cranial window in in vivo mouse brain imaging experiments[50], we placed a number 1.5 cover glass (0.16 to 0.19 mm thickness) tilted at 3° on top of the brain slices. Before imaging, we adjusted the correction collar of the objective lens to correct for spherical aberration introduced by a 0.17-mm-thick cover glass.

We assessed the accuracy of CoCoA in estimating optical aberration through a comparative analysis of the wavefront outputs from CoCoA and from DWS. Applying the corresponding corrective wavefronts to the DM (Fig. 2a), we also compared their performance in improving image quality. After one round of correction, CoCoA and DWS generated similar corrective wavefronts (insets for DWS AO [1] and CoCoA [1], Fig. 2b) and both led to significant improvements in signal and resolution, especially for fine synaptic features (white arrowheads, insets for DWS AO [1] and CoCoA [1], Fig. 2b). However, CoCoA's wavefront correction resulted in slightly inferior performance

compared with DWS, as indicated by the higher residual aberration (as measured by DWS after applying DWS [1] and CoCoA [1] to the DM; Fig. 2c) and the lower image contrast metric (bottom right, Fig. 2c). To further improve CoCoA's performance, we carried out iterative aberration corrections by inputting to CoCoA the 3D image stack acquired after applying the corrective wavefront from CoCoA of the previous round. Our results show that the performance of CoCoA gradually improved over three iterations, leading to comparable image quality with DWS AO (Fig. 2b). We also found the residual aberration after each iteration to decrease over CoCoA iterations, while DWS AO allowed diffraction-limited performance (as defined by the Rayleigh limit) after the second iteration (Fig. 2c).

Additionally, we evaluated the resolution improvement in the spatial-frequency domain by analysing the Fourier transform of the maximal intensity projection (MIP) image of aberration-corrected image stacks. Aberration correction, using corrective wavefront acquired through either DWS or CoCoA, led to larger magnitudes in high spatial-frequency range (that is, away from the origins in the 2D spatial-frequency representations; Fig. 2d, left panels). The recovery of high spatial-frequency information can also be easily appreciated from the radially averaged line power spectral density profiles (Fig. 2d, right panels). After only one iteration, both DWS and CoCoA corrections significantly increased the power over a broad spatial-frequency range when compared with 'No AO'. Compared with DWS [1], CoCoA [1] increased spectral power slightly less in the mid spatial-frequency region but had similar improvement at the high spatial-frequency end (inset in dashed box, Fig. 2d). After two iterations, CoCoA [2] and DWS [2] showed no perceivable difference. Quantitative Fourier ring correlation analyses showed similar improvements in resolution both laterally (Supplementary Fig. 10) and axially (Supplementary Fig. 11). These findings are consistent with residual aberration comparison and indicate that CoCoA's estimation of wavefront aberration is highly accurate.

We then investigated how the 3D structure output by CoCoA approximated the structure in real life. Because the ground-truth structural information is not available to us, we compared the structural output from CoCoA with those obtained via deconvolution, a widely applied technique that reassigns out-of-focus photons back to their sources and enhances high spatial-frequency information. We applied blind and non-blind deconvolutions based on the RLD algorithm[42,43] on the 'No AO' image stack used as input to CoCoA. In blind RLD, an estimated PSF obtained from a maximum likelihood algorithm (Methods) was used. In non-blind RLD, the aberrated PSF from the measured aberration by DWS was directly utilized, which should lead to the most accurate deconvolution. Therefore, we used the non-blind RLD output as the standard for comparison.

Occasionally, in locations with low brightness, CoCoA encountered difficulties in accurately depicting the dim and fine features that are visible in both the DWS AO image stack and non-blind RLD structure (for example, white arrowheads in the second row, Fig. 2e) or hallucinated structures that were absent from the non-blind RLD output (for example, white arrowheads in the third row, Fig. 2e; also see Supplementary Note for relevant discussion on post-processing). Overall, however, the morphology of dendrites and dendritic spines from the CoCoA output was highly consistent with the non-blind RLD output, and the axial locations of both CoCoA and non-blind RLD outputs agree well with the two-photon fluorescence image stack (second column, Fig. 2e). In contrast, blind RLD reconstruction led to much noisier features, from which the sample structure cannot be ascertained with high confidence. Therefore, both being software-only algorithms, CoCoA outperformed blind RLD. Furthermore, CoCoA achieved similar performance in structural recovery to that of non-blind RLD.

Characterizing performance limits by SNR and SBR

Although CoCoA succeeded in aberration estimation and structural recovery from the example images acquired from fixed brain slices, biological imaging often suffers from low SNR (Methods) and SBR (Supplementary Fig. 12). This is particularly true when imaging living organisms, where dim fluorophores and factors such as photodamage, photobleaching and short exposure time (for example, during time-lapse imaging) reduce the number of photons collected per pixel. For widefield fluorescence microscopy, larger out-of-focus fluorescence of thicker samples also leads to higher background. For all computational imaging approaches including CoCoA, images of low SNR and SBR pose challenges for their performance. Therefore, we investigated the minimum SNR and SBR thresholds required for CoCoA to be effective, before applying it for in vivo imaging experiments.

To control SNR, we introduced a fixed amount of aberration using the DM but adjusted the post-objective power, acquiring images of increasing SNRs at higher power (Fig. 3a). For primary vertical coma with a 0.15λ root mean square (r.m.s.) value, at very low SNR values (for example, 2.13; first column, Fig. 3a), there were not enough fluorescence photons to visualize features in our widefield images. Unsurprisingly, CoCoA also failed in structural recovering (first column, Fig. 3b). When SNR of the neuronal structures increased to 3.39, dendrites and dendritic spines could be visualized in the widefield MIP images (second column, Fig. 3a). However, CoCoA still failed to estimate the aberration or reveal the underlying structural features (second column, Fig. 3b). This was likely because even though signals of the in-focus features were sufficient for their visualization in MIP images, when out of the focal plane, the signals from these features were too noisy to be used by CoCoA for aberration estimation and structural retrieval. When the SNR increased to ~4, the performance of CoCoA markedly improved, with dendritic and synaptic features successfully retrieved (third column, Fig. 3a,b).

We quantified the performance of CoCoA using the Pearson correlation coefficient (PCC) and the Earth Mover's Distance (EMD)[51,52]. Using structures extracted by CoCoA from an aberration-free 3D image stack of high SNR as reference, PCC measures the correlation between CoCoA-reconstructed structures from aberrated image stacks and the reference, while EMD measures the distance between the two reconstructions by solving an optimal transport problem (Methods). PCC- and EMD-based quantifications confirmed the rapid performance improvement with the increase of SNR as observed by eye, with PCC increasing and EMD decreasing precipitously when SNR crosses a cutoff threshold value (Fig. 3c,d). Using two-segment piecewise linear fits on the PCC and EMD analysis, we found a cutoff SNR of 3.6 for this aberration, above which CoCoA provides robust structural recovery. The same cutoff also applied to aberration estimation (Fig. 3e). Below the cutoff, CoCoA erroneously returned non-zero coefficients for many non-primary-vertical-coma Zernike modes (grey symbols and lines, Fig. 3e; blue symbols and lines are the average of grey symbols and lines). Above the SNR cutoff, CoCoA accurately predicted the coefficient of primary vertical coma applied to the system (dashed black line at 0.15λ, Fig. 3e) and the coefficients for the other modes were effectively zero.

Furthermore, we tested another aberration mode, primary vertical astigmatism, also at 0.15λ r.m.s. value. Using the same quantification process, we found a cutoff SNR value of 4.5 (Fig. 3f–h). Together, these results indicate that CoCoA performs with high accuracy when the in-focus fluorescence features had 10–20 photons per pixel by assuming a Poisson distribution.

To experimentally control SBR levels, we introduced incrementally increasing aberration using the DM, from 0 to 0.31λ r.m.s. by 0.04λ r.m.s. steps. For each r.m.s. value, we applied three different mixed-mode aberrations with randomly generated Zernike coefficients. As the aberration increased, we observed a degradation in image quality and reduction in SBR (Fig. 4a). Above 0.2λ r.m.s., the 3D neuronal structures extracted by CoCoA started to severely deviate from those acquired at higher SBR (Fig. 4b).

https://doi.org/10.1038/s42256-024-00853-3

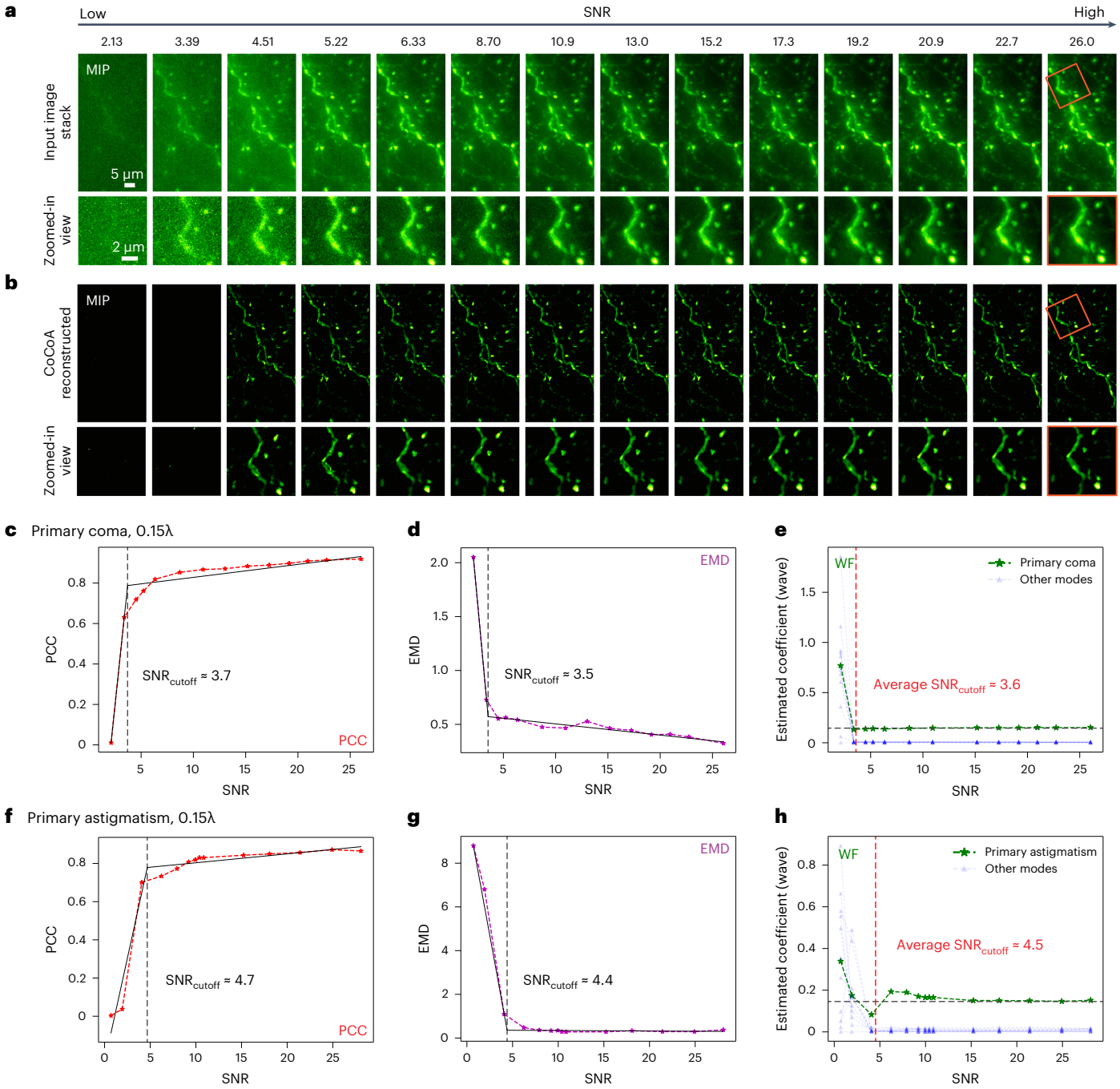

Fig. 3 | CoCoA's performance depends on SNR. a, MIPs of widefield image stacks in ascending order of SNR acquired with 0.15λ primary coma. Insets: zoomed-in views (orange box). All images individually normalized to [minimum, maximum]. **b**, MIPs of structural stacks reconstructed by CoCoA from images in **a**, individually normalized to [minimum, maximum]. **c**,**d**, PCC (**c**) and EMD (**d**) computed between CoCoA structure outputs from an unaberrated image stack and aberrated input image stacks in **b**. Two-segment piecewise linear fits (solid black lines) determine SNR cutoffs (vertical dashed black lines). **e**, CoCoA coefficients for primary coma (green symbols and lines) and other modes (grey symbols and lines) at different SNRs. Blue symbols and lines: average of other modes; ground truth, 0.15λ for primary coma (horizontal black dash-dot line) and 0 for all other modes. Vertical red dashed line: average SNR cutoff of **c** and **d**. **f**–**h**, Same as **c** (**f**), **d** (**g**) and **e** (**h**) but for 0.15λ primary astigmatism.

We plotted PCC and EMD against the given r.m.s. aberration and fitted the data points to two-segment piecewise linear curves. We carried out the same analyses for aberrations composed of low-order Zernike modes (Z_n^m, $2 \le n \le 4$; primary vertical coma, astigmatism and trefoil; Fig. 4c–f) or high-order modes ($n = 5$; secondary vertical coma, astigmatism and trefoil; Fig. 4g–j). For low-order aberrations, the cutoff aberration above which the reconstructed structure degraded severely was 0.19λ r.m.s. (Fig. 4c, d), a value above which the wavefront estimation error increased more steeply and became larger than 0.075λ, the Rayleigh limit (Fig. 4e). Similarly, for aberrations containing only higher-order modes, we identified a cutoff aberration (0.16λ r.m.s.; Fig. 4g–i) above which CoCoA gave rise to erroneous structures. The corresponding cutoff SBR for both low- and high-order aberrations was ~1.10 (Fig. 4), indicating that CoCoA successfully retrieved structural information when the signal was 10% stronger than the background. The fact that both low- and high-order aberrations led to the same cutoff SBR suggested that the performance of CoCoA was insensitive towards the orders of the Zernike modes.

https://doi.org/10.1038/s42256-024-00853-3

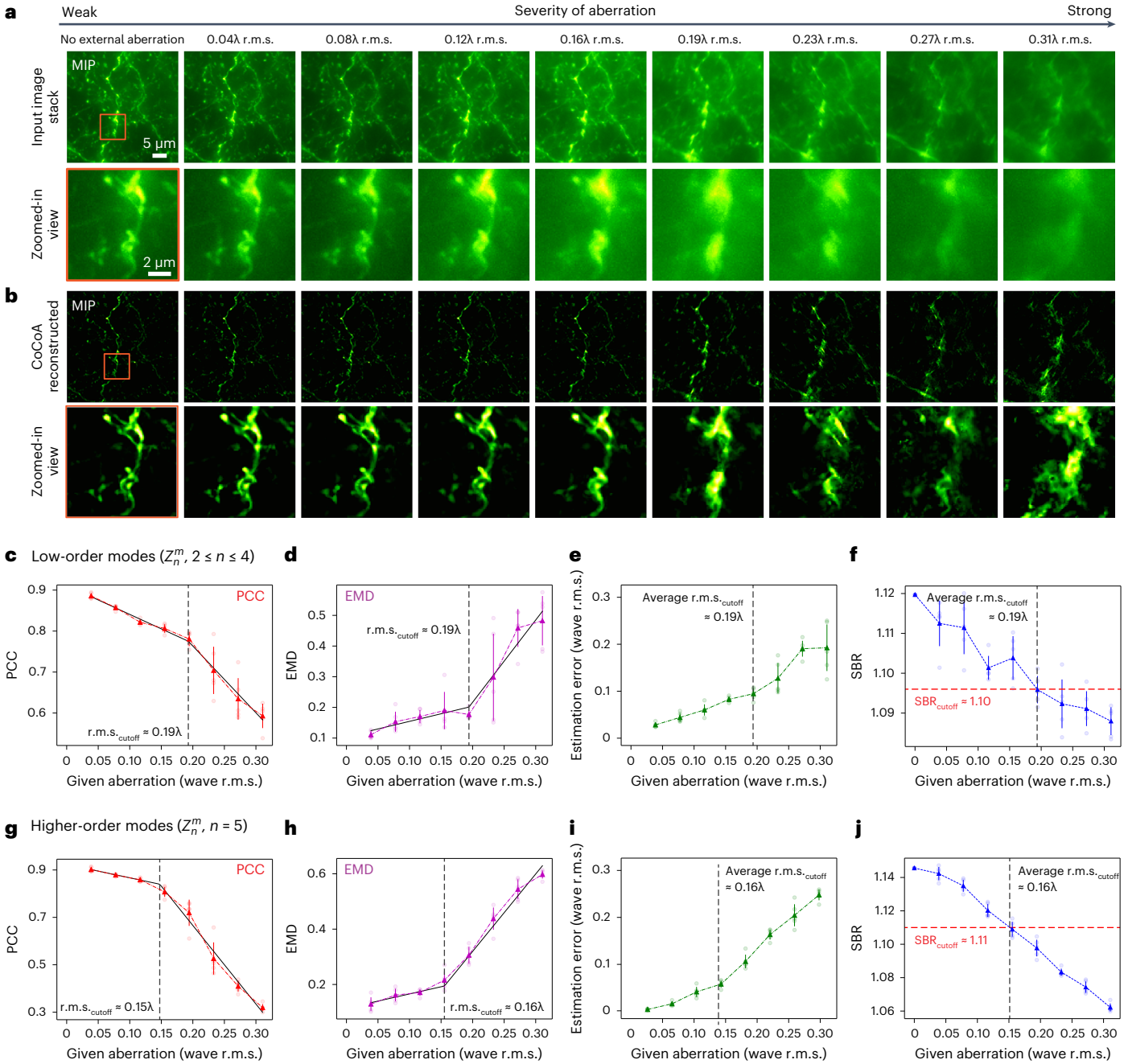

Fig. 4 | CoCoA's performance depends on SBR. a, MIPs of widefield image stacks measured with increasingly severe aberrations (mixed low-order modes). Insets: zoomed-in views (orange box). **b**, MIPs of structural stacks reconstructed by CoCoA from images in **a**. All MIPs in **b** individually normalized to [minimum, maximum]. **c**,**d**, PCC (**c**) and EMD (**d**) computed between CoCoA structure outputs from an unaberrated image stack and aberrated input image stacks in **b**. Two-segment piecewise linear fits (solid black lines) determine aberration r.m.s. cutoffs (vertical dashed black lines). **e**, Wavefront errors in r.m.s. between CoCoA-estimated and ground truth wavefront aberrations. **f**, SBR cutoff (horizontal red line) is determined from the average r.m.s. cutoff (vertical black lines in **e** and **f**). **g**–**j**, Same as in **c** (**g**), **d** (**h**), **e** (**i**) and **f** (**j**) but for mixed high-order modes. In **c**–**j**, data are presented as mean values ± s.d. ($n = 5$).

Biological samples contain features of different sizes and may vary in their fluorescence labelling density. To better understand how feature size and labelling density affect the performance limits of SNR and SBR, we carried out additional experiments on 3D tissue phantoms. These phantoms were prepared by mixing 1% agarose with fluorescent beads of either 500 nm or 2 μm diameter at varying densities. We tested phantoms with fractions of volume occupied by fluorescent beads ranging from 2.35×10^{-4} to 4.66×10^{-3} (for 500 nm beads) and from 5.11×10^{-4} to 2.75×10^{-3} (for 2 μm beads). We found SNR cutoffs ranging from 3.4 to 4.8 across the fluorescence volume fraction range and bead sizes (Supplementary Fig. 13), which were consistent with the cutoffs determined from brain slices (Fig. 3).

We also investigated bead phantoms with fluorescence volume fraction ranging from 4.96×10^{-3} to 1.70×10^{-2} (for 500 nm beads) and 4.78×10^{-3} to 1.52×10^{-2} (for 2 μm beads) (Supplementary Fig. 14). Similar to the simulation result (Supplementary Fig. 8e–h), the accuracy of structural retrieval, as quantified by PCC, was lowest for the densest sample (that is, 1.70×10^{-2} in Supplementary Fig. 14a), likely because denser samples had images of lower SBR and more overlap between neighbouring structures. However, aberration estimation accuracy and the SBR cutoff value were largely insensitive towards fluorescence volume fractions tested. For 500 nm beads, the SBR cutoff was as low as 1.03. This indicates that when SNRs are

https://doi.org/10.1038/s42256-024-00853-3

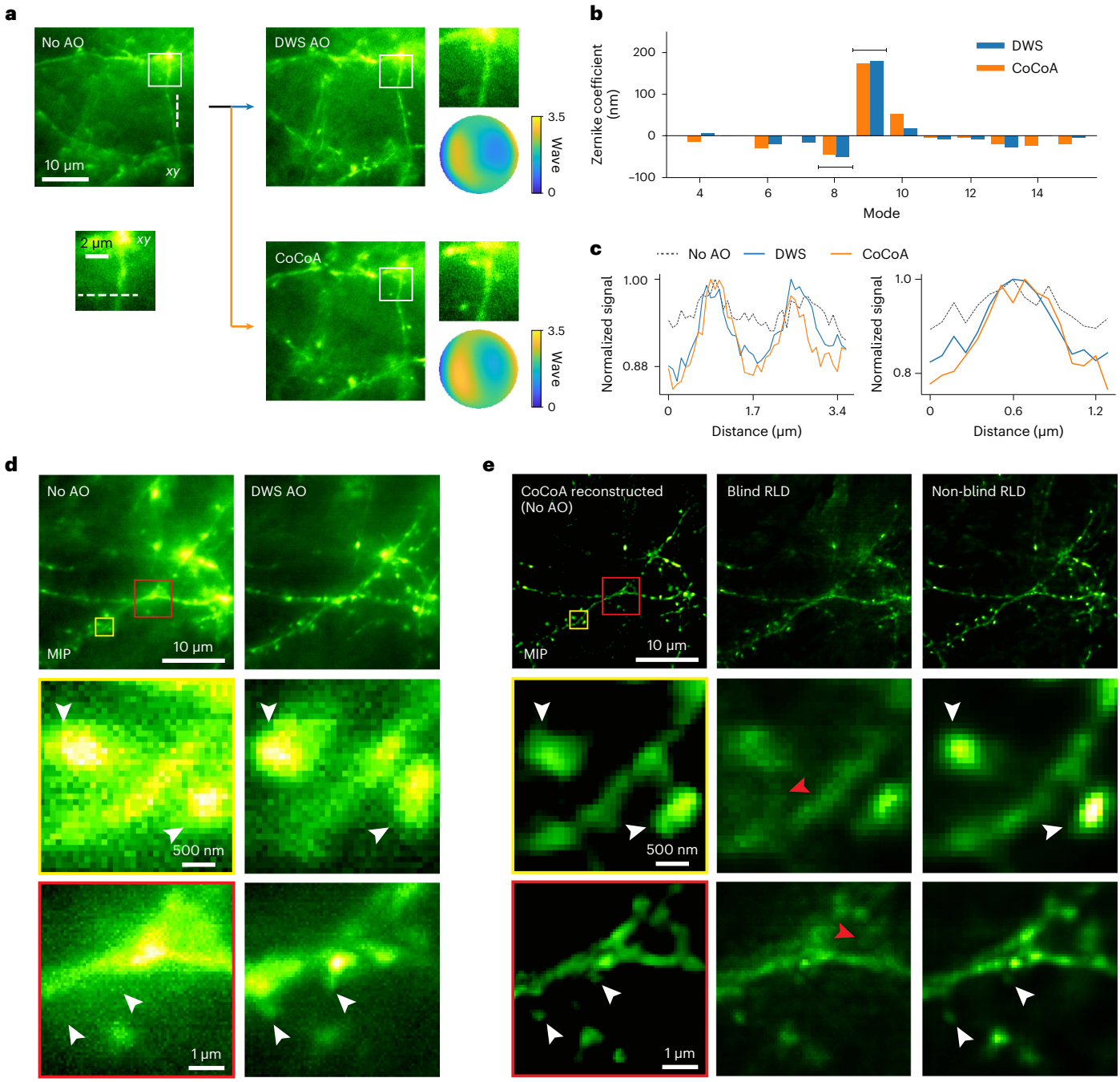

Fig. 5 | In vivo widefield imaging of a Thy1-GFP line M mouse brain with CoCoA. a, Single widefield image planes acquired without AO, with aberration correction by DWS and with aberration correction with CoCoA. Insets: zoomed-in view (white box) and corrective wavefronts. All images registered using the StackReg plugin in ImageJ and then individually normalized to [minimum, maximum]. **b**, Zernike coefficients of aberrations measured by DWS and CoCoA. Black brackets: primary coma modes. **c**, Lateral signal profiles along dashed white lines in **a**. Line profiles are normalized by their respective maximum values. **d**, MIPs of 4-μm-thick widefield image stacks measured without and with DWS AO and their zoomed-in views (yellow and red boxes). All images individually normalized to [minimum, maximum]. **e**, MIPs of 3D neuronal structures reconstructed by CoCoA, blind RLD and non-blind RLD using the 'No AO' image stack as the input. White arrowheads: synaptic and dendritic features; red arrowheads: artefactual structures. In vivo data were acquired 10–50 μm below dura.

sufficiently high, CoCoA performs well even for samples with very low SBR. We also found that the 2 μm beads had higher SBR cutoff values than 500 nm beads at the similar fluorescence volume fractions. Because structural features can be considered as continuous distributions of point sources and their images composed of continuously overlapping 3D PSFs centred on these point sources, out-of-focus signals of larger features contain comparatively less information on aberration, thus require higher SBR for aberration measurement and structural retrieval.

CoCoA for in vivo imaging of the mouse brain

Having validated CoCoA for imaging fixed brain slices and investigated its performance limits, we then applied it to high-resolution in vivo widefield imaging through a cranial window over the left cortex of a

Thy1-GFP line M mouse (Methods). We adjusted the correction collar of the objective lens to correct for spherical aberration introduced by the 0.17-mm-thick glass cranial window.

We first evaluated the accuracy of CoCoA in estimating optical aberration for in vivo mouse brain imaging by comparing its performance with DWS. Both CoCoA and DWS produced similar corrective wavefronts (Fig. 5a) with primary coma being the dominant Zernike mode (Fig. 5b), likely caused by a slight tilt of the cranial window away from being perpendicular to the optical axis of the objective. By applying the corrective wavefronts obtained from DWS and CoCoA onto the DM, we achieved higher resolution and contrast (quantitative Fourier ring correlation analysis in Supplementary Fig. 15), enabling better visualization of fine neuronal features, such as dendritic spines (Fig. 5a, white arrowheads; Fig. 5c, line signal profiles).

We next employed CoCoA to retrieve 3D neuronal structural information from the mouse brain in vivo. From the widefield images acquired without AO, CoCoA returned structural features such as dendritic spines that were consistent with the widefield images acquired with AO (Fig. 5d,e, white arrowheads). Using the same aberrated 'No AO' image stack as the input, we performed both blind and non-blind RLD (Fig. 5e, middle and right). Our results showed that CoCoA and non-blind RLD recovered similar synaptic structures (Fig. 5e, white arrowheads) while blind deconvolution resulted in artefactual structures (Fig. 5e, middle, red arrowheads).

The successful aberration estimation and structural recovery by CoCoA for in vivo imaging are to be expected, given that the SNR and SBR of the input image stacks (49.8 and 1.13, respectively; Fig. 5d) exceeded the cutoff values characterized previously. Notably, our experiments were conducted using illumination power within the typical range for in vivo widefield brain imaging experiments[53–55]. Therefore, our results indicate that CoCoA can be generally applied as a software-only approach to accurately estimate aberration and recover high-fidelity structures for in vivo brain imaging.

Discussion

Utilizing coordinate-based neural representations and incorporating a physical forward model to iteratively extract structural information, CoCoA is a new machine learning framework that enables simultaneous wavefront aberration estimation and 3D structural recovery from a single input, an aberrated widefield image stack. A self-supervised machine learning approach, CoCoA stands apart from existing supervised machine learning methods in that it does not require an external training dataset. Recovering structural features from aberrated images, CoCoA also does not require AO hardware such as a wavefront corrective device. Moreover, we believe our physics-informed framework can easily be extended to other imaging modalities.

CoCoA is distinct from digital AO strategies that were recently developed for aberration correction and image enhancement[56,57] of two-photon synthetic aperture microscopy and scanning light-field microscopy. Although elegant and effective, these methods iteratively estimate aberration from multi-view measurements obtained either through ptychographic scanning or a lenslet array. In contrast, the standard widefield microscopy images that CoCoA utilizes are single-view images, which cannot be used for aberration estimation by these previously published methods.

Using DWS AO and RLD, we validated the performance of CoCoA in accurately estimating optical aberration and recovering structural features. Successfully demonstrating the capabilities of CoCoA in imaging neuronal structures in the living mouse brain, our work represents a successful in vivo application of machine learning-based AO for 3D structural recovery in widefield microscopy.

Importantly, we conducted a detailed investigation into the performance limits of CoCoA, specifically in terms of SBR and SNR and determined their cutoff values required for successful CoCoA reconstruction. Our analyses suggest that there exists a fundamental lower limit on the amount of information contained in an image stack that is necessary for CoCoA to produce accurate wavefront estimation and structural information. These limits likely generally apply to all computational, including machine learning-based AO approaches.

Methods

Animal use

All animal experiments were conducted according to the National Institutes of Health guidelines for animal research. Procedures and protocols on mice were approved by the Institutional Animal Care and Use Committee at the University of California, Berkeley (AUP-2020-06-13343).

AO widefield fluorescence microscope

The AO widefield microscope had two working modes (Supplementary Fig. 2): widefield imaging mode and two-photon excitation (2PE) for AO mode. The switch between the two modes was achieved using a movable mirror (MM) controlled by an electric nanopositioning stage (SmarAct, modulator control system).

In the widefield imaging pathway (Supplementary Fig. 2a, MM out), illumination was delivered to the sample and the emitted fluorescence was recorded by a sCMOS camera. The output beam from a 488-nm continuous laser (Coherent, Sapphire LPX 488, 400 mW) was expanded 18 times by three beam expanders (two ×3, Thorlabs, GBE03-A; one ×2, Thorlabs GBE02-A) after passing through an acoustic-optic tunable filter (AOTF; AA Opto-Electronic, AOTFnC-400.650-TN). The illumination was then relayed to the sample by three achromatic lenses (L1, L2 and L3, focal lengths (FLs) = 150, 125 and 400 mm, respectively) and an objective lens (Nikon, CFI Apo LWD ×25, 1.1 NA and 2-mm WD). Emitted fluorescence was collected with the same objective. A dichroic mirror (D1, Semrock, Di-405/488/561/635-t3-25×36) was placed between L3 and the objective, reflecting illumination and transmitting collected fluorescence. The back focal plane of the objective was relayed to a DM (Iris AO, PTT489) by a pair of achromatic lenses (L4 and L5, FL = 400 and 175 mm, respectively). Fluorescence reflected by the DM was then focused and imaged on a sCMOS camera (Hamamatsu, Orca Flash 4.0) by three lenses (L6, L7 and L8, FLs = 300, 85 and 75 mm, respectively).

In the AO 2PE pathway (Supplementary Fig. 2b, MM in), the wavefront of a 2PE fluorescence guide was directly measured to determine artificial or sample-induced aberration. The output beam from a Ti:sapphire laser (Coherent, Chameleon Ultra II) was expanded 2 times by a beam expander (×2, Thorlabs GBE02-B) after being modulated by a Pockels Cell (ConOptics, 302RM). The 2PE beam was then scanned with a pair of galvanometer mirrors (Cambridge, H2105) that are optically conjugated with a pair of achromatic lenses (L12 and L11, FL = 85 mm). Another pair of achromatic lenses (L10 and L9) further conjugated the galvos to the DM. For wavefront sensing, the emitted 2PE fluorescence first followed the same path as in the widefield imaging mode. The MM was placed in to reflect the fluorescence after the DM. Being relayed by L11 and L12 and descanned by the galvanometer pair, the fluorescence was reflected by a dichroic mirror (D3, Semrock, Di02-R785-25×36) and relayed to an SH sensor by a pair of achromatic lenses (L13 and L14, FLs = 60 and 175 mm, respectively). The SH sensor was composed of a lenslet array (Advanced Microoptic Systems GmbH) conjugated to the objective back pupil plane and a camera (Hamamatsu, Orca Flash 4.0) at the focal plane of the lenslet array. Focal shifts in the SH pattern were used to calculate wavefront distortion. The corrective pattern could be then determined and applied to the DM to correct the measured aberration. When needed, two-photon fluorescence imaging was enabled by placing a dichroic mirror (D1, Semrock, Di02-R785-25×36) into the light path, which reflected the emitted fluorescence to be focused on a photomultiplier tube (Hamamatsu, H7422-40). Imaging parameters can be found in Supplementary Table 2.

System correction and wavefront sensor calibration

In all experiments, before imaging biological samples, system aberration caused by optics imperfections and/or misalignment was measured in the widefield light path using the phase retrieval approach based on the Gerchberg–Saxton algorithm[58] from a 3D image stack of a 200-nm-diameter fluorescent bead and corrected by the DM. Fluorescence from a 7.6 × 7.6 μm^2 field of 2-μm-diameter fluorescent beads (ThermoFisher Scientific FluoSpheres Carboxylate-Modified Microspheres, yellow-green 505/515) on a glass slide were two-photon excited. After descanning and reflecting off the DM with system aberration correction, the recorded pattern on the SH sensor of the fluorescence wavefront was used as the aberration-free reference pattern for wavefront measurement.

Beads sample on glass slide

The 2-μm-diameter fluorescent bead stock solution was diluted (1:500 in deionized water) and then pipetted onto a microscope glass slide precoated with poly-L-lysine hydrobromide (10 mg ml^{-1}; Sigma-Aldrich, P7890). The same method was followed to prepare 200-nm-diameter fluorescent beads sample for the validation of CoCoA in imaging sub-diffraction-limited fluorescent beads (1:10k dilution).

Fixed mouse brain slices preparation

We prepared brain slices from a Thy1-GFP line M transgenic mouse (The Jackson Laboratory, stock 007788). After being deeply anaesthetized with isoflurane (Piramal), we performed a standard transcardial perfusion first with phosphate-buffered saline (Invitrogen) followed by 4% paraformaldehyde (Electron Microscopy Sciences). We then collected the mouse brain and immersed it in 2% paraformaldehyde and 15% sucrose in PBS solution overnight at 4 °C. After that, the immersion solution was replaced with 30% sucrose in PBS, and the brain was stored at 4 °C. After another 24 h, the mouse brain was cut to 100-μm-thick slices on a microtome (Thermo Scientific, Microm HM430). Brain slices were then placed on microscope glass slides and allowed to dry for 1 h. Cover glass (Fisherbrand, number 1.5) with mounting medium (Vectashield HardSet Antifade mounting medium, H-1400) was then placed on top of the glass slides with brain slices. Slices were ready for imaging after the mounting medium completely hardened.

Cranial window implantation and in vivo mouse brain imaging

All Thy1-GFP line M mice (The Jackson Laboratory, stock 007788) were around four months old at the time of cranial window installation. The mice were deeply anaesthetized under isoflurane (2.0% v/v in O_2) during the whole surgery. A craniotomy (3.5 mm in diameter) was created over the left cortex with dura intact. A cranial window was made by gluing (Norland 68 Optical Adhesive) together a glass ring (inner diameter, 3 mm; outer diameter, 4.5 mm) and a glass disk (diameter, 3.5 mm), both were laser cut from standard number 1.5 microscope cover glass (Fisherbrand). The cranial window was embedded into the craniotomy and the glass ring was glued onto the skull by Vetbond (Vetbond, 3M). A titanium head-bar was then fixed on the skull with Vetbond and fast curing orthodontic acrylic resin (Lang Dental Mfg). In vivo mouse brain imaging was conducted under light isoflurane anaesthesia (0.5 to 1.0% v/v in O_2) 2 h after surgery.

Calculating signal-to-background and signal-to-noise ratios

The calculation of SBR follows four steps (Supplementary Fig. 12): (1) denoise the image stack using a 3D low-pass Gaussian kernel; (2) remove DC components and low-frequency background fluctuations using a 3D high-pass Gaussian kernel; (3) fit the image stack with a two-component Gaussian mixture model and classify the voxels into two groups (that is, background and signal); and (4) compute SBR as the ratio of the mean of the signal voxels to the mean of the background voxels.

To compute SNR, we first assessed the gain of the CMOS camera to convert grayscale pixel values p to photon count c per pixel. Assuming a linear relationship between the two quantities, the pixel value can be expressed as $p = \beta c$, where β represents the gain in pixel value per photon count. Considering that c follows a Poisson random distribution, with its variance Var[c] equal to its mean $E[c]$, we derived β to be the ratio of Var[p] to $E[p]$. We conducted a characterization of the gain at different power levels and observed the constant gain of 2.19.

Using the signal voxels from the SBR analysis, we calculated the SNR as

$$\mathrm{SNR} = \frac{\bar{y}/\beta}{\sqrt{\bar{y}/\beta + (n_r/\beta)^2}} \tag{5}$$

where β is the gain in pixel values per photon count, y denotes the set of signal voxels in the image stack and n_r represents the readout noise calculated as the standard deviation of pixel values in frames acquired without light exposure to the camera.

PCC and EMD calculations

To quantify the similarity between two structural reconstructions, we employed two metrics: PCC and EMD. PCC is defined as the normalized inner product of the two reconstructions:

$$\mathrm{PCC}(s_1, s_2) = \frac{\sum_i (s_{1i} - \overline{s_1})(s_{2i} - \overline{s_2})}{\sqrt{\sum_i (s_{1i} - \overline{s_1})^2 \sum_i (s_{2i} - \overline{s_2})^2}}. \tag{6}$$

For EMD, we computed a Monte Carlo approximation of the p-sliced Wasserstein distance[59], with $p = 2$ and 200 projections used for the approximation.

Blind and non-blind RLD implementation

Both blind and non-blind deconvolution processes were performed using a GPU-accelerated Python implementation of RLD[41]. Both non-blind and blind RLD were applied to image stacks acquired without AO correction. Non-blind RLD utilized the 3D PSF calculated from the wavefront aberration measured from DWS. The non-blind reconstructions were achieved with 500 iterations (87 s of computation) for the brain slice sample (Fig. 2) and 2000 iterations (445 s of computation) for in vivo mouse brain (Fig. 5) of the RLD algorithm.

Blind RLD first estimated the 3D PSF using 100 iterations of the maximum likelihood algorithm utilizing MATLAB's deconvblind function[60] and then deconvolved the image stack with the estimated PSF using the same number of RLD iterations as the non-blind case. Consequently, blind RLD took substantially longer than non-blind RLD: estimating PSF took 1141 s for the brain slice sample (Fig. 2) and approximately 1.25 h for the in vivo mouse brain (Fig. 5). The deconvolution step took the same amount of time as non-blind RLD above. Therefore, the total computation time of blind RLD was 1,228 s and 1.37 h for the slice and in vivo imaging, respectively.

Ethics

All animal experiments were conducted according to the National Institutes of Health guidelines for animal research. Procedures and protocols on mice were approved by the Institutional Animal Care and Use Committee at the University of California, Berkeley (AUP-2020-06-13343).

Reporting summary

Further information on research design is available in the Nature Portfolio Reporting Summary linked to this article.

Data availability

The data used for the results in the paper, for example, fixed mouse brain slice (Fig. 2) and mouse brain in vivo (Fig. 5), are available at

https://github.com/iksungk/CoCoA (ref. 61). Due to repository storage limitations, please email the corresponding authors (I.K. and Q.Z.) for access to the rest of the data for both the paper and supplementary material.

Code availability

Code is publicly available at https://github.com/iksungk/CoCoA (ref. 61).

References

1. Ji, N. Adaptive optical fluorescence microscopy. *Nat. Methods* **14**, 374–380 (2017).
2. Hampson, K. M. et al. Adaptive optics for high-resolution imaging. *Nat. Rev. Methods Primer* **1**, 68 (2021).
3. Zhang, Q. et al. Adaptive optics for optical microscopy [invited]. *Biomed. Opt. Express* **14**, 1732 (2023).
4. Rueckel, M., Mack-Bucher, J. A. & Denk, W. Adaptive wavefront correction in two-photon microscopy using coherence-gated wavefront sensing. *Proc. Natl Acad. Sci. USA* **103**, 17137–17142 (2006).
5. Cha, J. W., Ballesta, J. & So, P. T. C. Shack-Hartmann wavefront-sensor-based adaptive optics system for multiphoton microscopy. *J. Biomed. Opt.* **15**, 046022 (2010).
6. Aviles-Espinosa, R. et al. Measurement and correction of in vivo sample aberrations employing a nonlinear guide-star in two-photon excited fluorescence microscopy. *Biomed. Opt. Express* **2**, 3135 (2011).
7. Azucena, O. et al. Adaptive optics wide-field microscopy using direct wavefront sensing. *Opt. Lett.* **36**, 825–827 (2011).
8. Wang, K. et al. Rapid adaptive optical recovery of optimal resolution over large volumes. *Nat. Methods* **11**, 625–628 (2014).
9. Wang, K. et al. Direct wavefront sensing for high-resolution in vivo imaging in scattering tissue. *Nat. Commun.* **6**, 7276 (2015).
10. Paine, S. W. & Fienup, J. R. Machine learning for improved image-based wavefront sensing. *Opt. Lett.* **43**, 1235 (2018).
11. Asensio Ramos, A., De La Cruz Rodríguez, J. & Pastor Yabar, A. Real-time, multiframe, blind deconvolution of solar images. *Astron. Astrophys.* **620**, A73 (2018).
12. Nishizaki, Y. et al. Deep learning wavefront sensing. *Opt. Express* **27**, 240 (2019).
13. Andersen, T., Owner-Petersen, M. & Enmark, A. Neural networks for image-based wavefront sensing for astronomy. *Opt. Lett.* **44**, 4618 (2019).
14. Saha, D. et al. Practical sensorless aberration estimation for 3D microscopy with deep learning. *Opt. Express* **28**, 29044 (2020).
15. Wu, Y., Guo, Y., Bao, H. & Rao, C. Sub-millisecond phase retrieval for phase-diversity wavefront sensor. *Sensors* **20**, 4877 (2020).
16. Allan, G., Kang, I., Douglas, E. S., Barbastathis, G. & Cahoy, K. Deep residual learning for low-order wavefront sensing in high-contrast imaging systems. *Opt. Express* **28**, 26267 (2020).
17. Yanny, K., Monakhova, K., Shuai, R. W. & Waller, L. Deep learning for fast spatially varying deconvolution. *Optica* **9**, 96 (2022).
18. Hu, Q. et al. Universal adaptive optics for microscopy through embedded neural network control. *Light: Sci. Appl.* **12**, 270 (2023)
19. Lehtinen, J. et al. Noise2Noise: learning image restoration without clean data. In *Proc. 35th International Conference on Machine Learning* Vol. 80 (eds Dy, J. & Krause, A.) 2965–2974 (PMLR, 2018).
20. Krull, A., Buchholz, T.-O. & Jug, F. Noise2Void - learning denoising from single noisy images. In *Proc. 2019 IEEE/CVF Conference on Computer Vision and Pattern Recognition (CVPR)* 2124–2132 (IEEE, 2019); https://doi.org/10.1109/CVPR.2019.00223
21. Platisa, J. et al. High-speed low-light in vivo two-photon voltage imaging of large neuronal populations. *Nat. Methods* **20**, 1095–1103 (2023).
22. Li, X. et al. Real-time denoising enables high-sensitivity fluorescence time-lapse imaging beyond the shot-noise limit. *Nat. Biotechnol.* https://doi.org/10.1038/s41587-022-01450-8 (2022).
23. Eom, M. et al. Statistically unbiased prediction enables accurate denoising of voltage imaging data. *Nat. Methods* **20**, 1581–1592 (2022).
24. Ren, D., Zhang, K., Wang, Q., Hu, Q. & Zuo, W. Neural blind deconvolution using deep priors. In *Proc. 2020 IEEE/CVF Conference on Computer Vision and Pattern Recognition (CVPR)* 3338–3347 (IEEE, 2020); https://doi.org/10.1109/CVPR42600.2020.00340
25. Wang, F. et al. Phase imaging with an untrained neural network. *Light: Sci. Appl.* **9**, 77 (2020).
26. Bostan, E., Heckel, R., Chen, M., Kellman, M. & Waller, L. Deep phase decoder: self-calibrating phase microscopy with an untrained deep neural network. *Optica* **7**, 559 (2020).
27. Kang, I. et al. Simultaneous spectral recovery and CMOS micro-LED holography with an untrained deep neural network. *Optica* **9**, 1149 (2022).
28. Zhou, K. C. & Horstmeyer, R. Diffraction tomography with a deep image prior. *Opt. Express* **28**, 12872 (2020).
29. Sun, Y., Liu, J., Xie, M., Wohlberg, B. & Kamilov, U. CoIL: coordinate-based internal learning for tomographic imaging. *IEEE Trans. Comput. Imaging* **7**, 1400–1412 (2021).
30. Liu, R., Sun, Y., Zhu, J., Tian, L. & Kamilov, U. Recovery of continuous 3D refractive index maps from discrete intensity-only measurements using neural fields. *Nat. Mach. Intell.* **4**, 781–791 (2022).
31. Kang, I. et al. Accelerated deep self-supervised ptycho-laminography for three-dimensional nanoscale imaging of integrated circuits. *Optica* **10**, 1000–1008 (2023).
32. Chan, T. F. & Chiu-Kwong, W. Total variation blind deconvolution. *IEEE Trans. Image Process.* **7**, 370–375 (1998).
33. Levin, A., Weiss, Y., Durand, F. & Freeman, W. T. Understanding and evaluating blind deconvolution algorithms. In *Proc. 2009 IEEE Conference on Computer Vision and Pattern Recognition* 1964–1971 (IEEE, 2009); https://doi.org/10.1109/CVPR.2009.5206815
34. Perrone, D. & Favaro, P. Total variation blind deconvolution: the devil is in the details. In *Proc. 2014 IEEE Conference on Computer Vision and Pattern Recognition* 2909–2916 (IEEE, 2014); https://doi.org/10.1109/CVPR.2014.372
35. Jin, M., Roth, S. & Favaro, P. in *Computer Vision – ECCV 2018. ECCV 2018. Lecture Notes in Computer Science* Vol. 11211 (eds Ferrari, V. et al.) 694–711 (Springer, 2018).
36. Hornik, K., Stinchcombe, M. & White, H. Multilayer feedforward networks are universal approximators. *Neural Netw.* **2**, 359–366 (1989).
37. Cybenko, G. Approximation by superpositions of a sigmoidal function. *Math. Control Signals Syst.* **2**, 303–314 (1989).
38. Tewari, A. et al. Advances in neural rendering. In *ACM SIGGRAPH 2021 Courses*, 1–320 (Association for Computing Machinery, 2021).
39. Tancik, M. et al. in *Advances in Neural Information Processing Systems* Vol. 33 (eds Larochelle, H. et al.) 7537–7547 (Curran Associates, 2020).
40. Mildenhall, B. et al. NeRF: representing scenes as neural radiance fields for view synthesis. *Commun. ACM* **65**, 99–106 (2022).
41. Perdigao, L., Shemilt, L. A. & Nord, N. rosalindfranklininstitute/RedLionfish v.0.9. *Zenodo* https://doi.org/10.5281/zenodo.7688291 (2023).
42. Richardson, W. H. Bayesian-based iterative method ofimage restoration*. *J. Opt. Soc. Am.* **62**, 55 (1972).
43. Lucy, L. B. An iterative technique for the rectification of observed distributions. *Astron. J.* **79**, 745 (1974).
44. Sitzmann, V. et al. Scene representation networks: continuous 3D-structure-aware neural scene representations. In *Proc. 33rd International Conference on Neural Information Processing Systems* Vol. 32 (eds Wallach, H. et al.) 1121–1132 (Curran Associates, 2019).

45. Martel, J. N. P. et al. ACORN: adaptive coordinate networks for neural scene representation. *ACM Trans. Graph.* **40**, 1–13 (2021).
46. Zhao, H., Gallo, O., Frosio, I. & Kautz, J. Loss functions for image restoration with neural networks. *IEEE Trans. Comput. Imaging* **3**, 47–57 (2017).
47. Kang, I., Zhang, F. & Barbastathis, G. Phase extraction neural network (PhENN) with coherent modulation imaging (CMI) for phase retrieval at low photon counts. *Opt. Express* **28**, 21578 (2020).
48. Kingma, D. P. & Ba, J. Adam: a method for stochastic optimization. Preprint at https://doi.org/10.48550/arXiv.1412.6980 (2017).
49. Paszke, A. et al. PyTorch: an imperative style, high-performance deep learning library. In *Proc. 33rd International Conference on Neural Information Processing Systems* (eds Wallach, H. M. et al.) 721 (Curran Associates, 2019).
50. Turcotte, R., Liang, Y. & Ji, N. Adaptive optical versus spherical aberration corrections for in vivo brain imaging. *Biomed. Opt. Express* **8**, 3891–3902 (2017).
51. Kolouri, S., Park, S. R., Thorpe, M., Slepcev, D. & Rohde, G. K. Optimal mass transport: signal processing and machine-learning applications. *IEEE Signal Process Mag.* **34**, 43–59 (2017).
52. Villani, C. *Topics in Optimal Transportation* Vol. 58 (American Mathematical Society, 2021).
53. Turcotte, R. et al. Dynamic super-resolution structured illumination imaging in the living brain. *Proc. Natl Acad. Sci. USA* **116**, 9586–9591 (2019).
54. Li, Z. et al. Fast widefield imaging of neuronal structure and function with optical sectioning in vivo. *Sci. Adv.* **6**, eaaz3870 (2020).
55. Zhang, Q., Pan, D. & Ji, N. High-resolution in vivo optical-sectioning widefield microendoscopy. *Optica* **7**, 1287 (2020).
56. Zhao, Z. et al. Two-photon synthetic aperture microscopy for minimally invasive fast 3D imaging of native subcellular behaviors in deep tissue. *Cell* **186**, 2475–2491.e22 (2023).
57. Wu, J. et al. Iterative tomography with digital adaptive optics permits hour-long intravital observation of 3D subcellular dynamics at millisecond scale. *Cell* **184**, 3318–3332.e17 (2021).
58. Gerchberg, R. W. A practical algorithm for the determination of plane from image and diffraction pictures. *Optik* **35**, 237–246 (1972).
59. Flamary, R. et al. POT: Python optimal transport. *J. Mach. Learn. Res.* **22**, 1–8 (2021).
60. Holmes, T. J. et al. in *Handbook of Biological Confocal Microscopy* (ed. Pawley, J. B.) 389–402 (Springer, 1995).
61. Kang, I., Zhang, Q., Yu, S. & Ji, N. iksungk/CoCoA: Github CoCoA WF 1.0.0. *Zenodo* https://doi.org/10.5281/zenodo.10655781 (2024).

Acknowledgements

This work was supported by the Weill Neurohub (N.J.) and National Institutes of Health (U01NS118300) (I.K., Q.Z. and N.J.).

Author contributions

I.K. and Q.Z. conceived of the project. N.J. supervised the project. I.K., Q.Z. and N.J. designed experiments. I.K. developed the CoCoA method with input from S.X.Y. Q.Z. prepared samples. Q.Z. and I.K. acquired data and prepared figures. I.K., Q.Z. and N.J. wrote the paper.

Competing interests

The authors declare no competing interests.

Additional information

Supplementary information The online version contains supplementary material available at https://doi.org/10.1038/s42256-024-00853-3.

Correspondence and requests for materials should be addressed to Iksung Kang or Qinrong Zhang.

Peer review information *Nature Machine Intelligence* thanks Xi Chen and Jiamin Wu for their contribution to the peer review of this work.

nature portfolio

Corresponding author(s): Iksung Kang, Qinrong Zhang

Last updated by author(s): Apr 24, 2024

Reporting Summary

Nature Portfolio wishes to improve the reproducibility of the work that we publish. This form provides structure for consistency and transparency in reporting. For further information on Nature Portfolio policies, see our Editorial Policies and the Editorial Policy Checklist.

Statistics

For all statistical analyses, confirm that the following items are present in the figure legend, table legend, main text, or Methods section.

n/a	Confirmed	
☐	☒	The exact sample size (*n*) for each experimental group/condition, given as a discrete number and unit of measurement
☒	☐	A statement on whether measurements were taken from distinct samples or whether the same sample was measured repeatedly
☒	☐	The statistical test(s) used AND whether they are one- or two-sided *Only common tests should be described solely by name; describe more complex techniques in the Methods section.*
☒	☐	A description of all covariates tested
☒	☐	A description of any assumptions or corrections, such as tests of normality and adjustment for multiple comparisons
☐	☒	A full description of the statistical parameters including central tendency (e.g. means) or other basic estimates (e.g. regression coefficient) AND variation (e.g. standard deviation) or associated estimates of uncertainty (e.g. confidence intervals)
☒	☐	For null hypothesis testing, the test statistic (e.g. *F*, *t*, *r*) with confidence intervals, effect sizes, degrees of freedom and *P* value noted *Give P values as exact values whenever suitable.*
☒	☐	For Bayesian analysis, information on the choice of priors and Markov chain Monte Carlo settings
☒	☐	For hierarchical and complex designs, identification of the appropriate level for tests and full reporting of outcomes
☒	☐	Estimates of effect sizes (e.g. Cohen's *d*, Pearson's *r*), indicating how they were calculated

Our web collection on statistics for biologists contains articles on many of the points above.

Software and code

Policy information about availability of computer code

Data collection	Data collection was performed by customized code.
Data analysis	Customized code was developed to analyze data using Python 3.6.0 and Pytorch 1.8.0. The code with more details can be found in our public repository (https://github.com/iksungk/CoCoA).

For manuscripts utilizing custom algorithms or software that are central to the research but not yet described in published literature, software must be made available to editors and reviewers. We strongly encourage code deposition in a community repository (e.g. GitHub). See the Nature Portfolio guidelines for submitting code & software for further information.

Data

Policy information about availability of data

All manuscripts must include a data availability statement. This statement should provide the following information, where applicable:

- Accession codes, unique identifiers, or web links for publicly available datasets
- A description of any restrictions on data availability
- For clinical datasets or third party data, please ensure that the statement adheres to our policy

The data used for the results, e.g., fixed mouse brain slice (Figure 2) and mouse brain in vivo (Figure 5), are available at our public repository. Due to repository storage limitations, please email the corresponding authors for access to the rest of the data for both the manuscript and supplementary material.

Human research participants

Policy information about studies involving human research participants and Sex and Gender in Research.

Reporting on sex and gender	N/A
Population characteristics	N/A
Recruitment	N/A
Ethics oversight	N/A

Note that full information on the approval of the study protocol must also be provided in the manuscript.

Field-specific reporting

Please select the one below that is the best fit for your research. If you are not sure, read the appropriate sections before making your selection.

☒ Life sciences ☐ Behavioural & social sciences ☐ Ecological, evolutionary & environmental sciences

For a reference copy of the document with all sections, see nature.com/documents/nr-reporting-summary-flat.pdf

Life sciences study design

All studies must disclose on these points even when the disclosure is negative.

Sample size	We used a single Thy1-GFP line M mouse to evaluate our algorithm's performance in in vivo structural imaging.
Data exclusions	No data were excluded.
Replication	The presented results were able to be reproduced by running the customized code available from our public repository.
Randomization	Randomization was not necessary because our experiments did not include any sample/organism/participant allocation into experimental groups.
Blinding	Blinding was not necessary because our experiments did not include any group allocation during data allocation and analysis.

Reporting for specific materials, systems and methods

We require information from authors about some types of materials, experimental systems and methods used in many studies. Here, indicate whether each material, system or method listed is relevant to your study. If you are not sure if a list item applies to your research, read the appropriate section before selecting a response.

Materials & experimental systems

n/a	Involved in the study
☒	☐ Antibodies
☒	☐ Eukaryotic cell lines
☒	☐ Palaeontology and archaeology
☐	☒ Animals and other organisms
☒	☐ Clinical data
☒	☐ Dual use research of concern

Methods

n/a	Involved in the study
☒	☐ ChIP-seq
☒	☐ Flow cytometry
☒	☐ MRI-based neuroimaging

Animals and other research organisms

Policy information about studies involving animals; ARRIVE guidelines recommended for reporting animal research, and Sex and Gender in Research

Laboratory animals	Mouse (Thy1-GFP line M, 2-3 months old), light cycle - On: 7am, Off: 7pm, humidity: 40-60%, ambient temperature: 67-70°F.
Wild animals	No wild animals were used in the study.

Reporting on sex	Gender or sex was not included as a covariate in our analysis at any stage of the study, as sex- and gender-based analysis is not relevant to the study.
Field-collected samples	No field collected samples were used in the study.
Ethics oversight	All animal experiments were conducted according to the National Institutes of Health guidelines for animal research. Procedures and protocols on mice were approved by the Institutional Animal Care and Use Committee at the University of California, Berkeley (AUP-2020-06-13343).

Note that full information on the approval of the study protocol must also be provided in the manuscript.